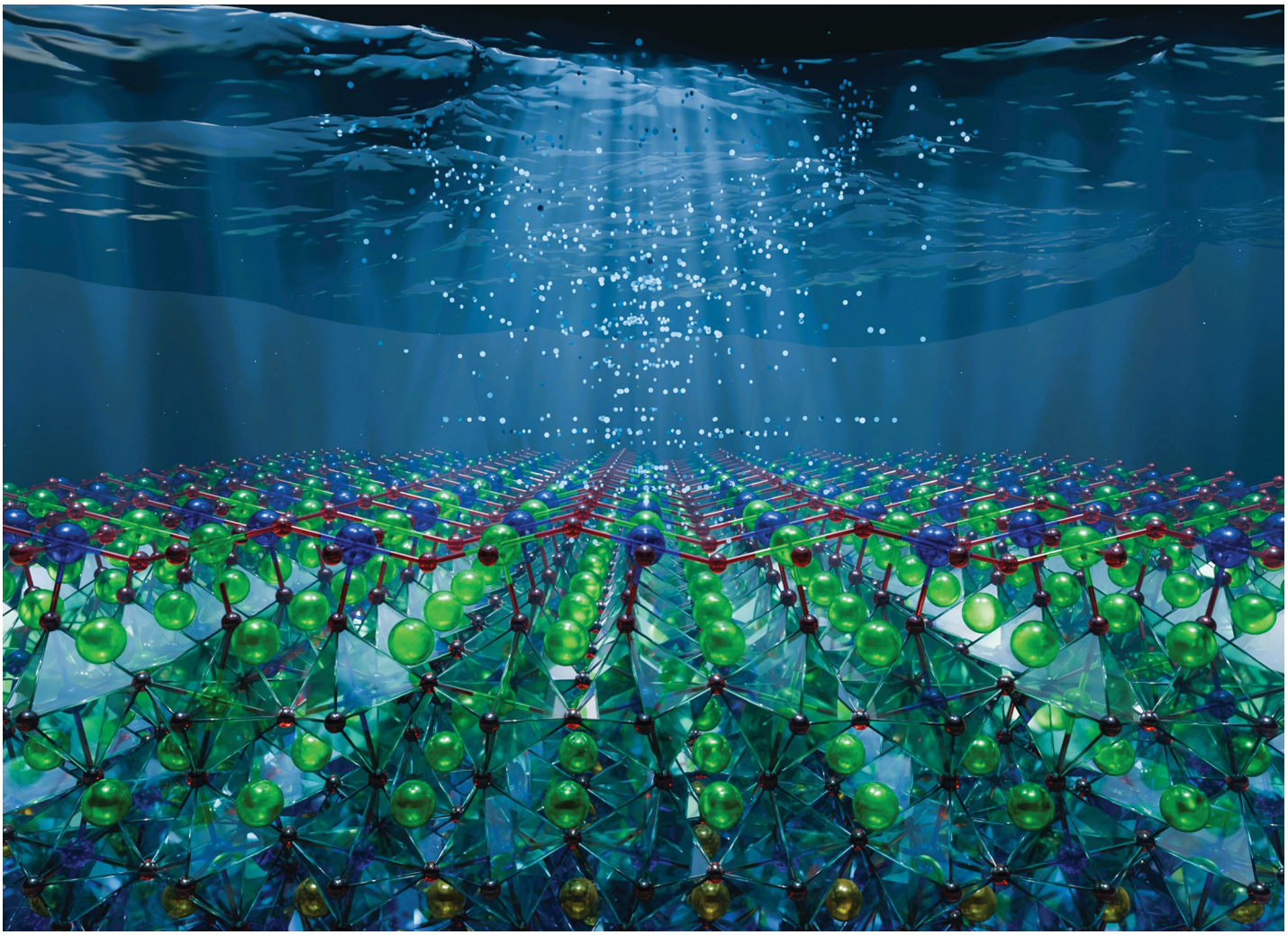

Showcasing research from Professor Sato's laboratory, Kyoto University and Professor Onishi, Kobe University, Japan.

Dopant distributions and band-edge positions in Sr-doped $NaTaO_3$: a first-principles study

In this work, we performed first-principles calculations on an archetypal photocatalyst, Sr-doped $NaTaO_3$, to connect dopant distributions with band-edge modulation. We show that short Sr–Sr separations are thermodynamically favoured, explaining the experimentally suggested near-surface Sr enrichment. Sr-rich layers form in-gap states and shift both valence- and conduction-band edges upward, creating a built-in electric field that promotes charge separation and suppresses recombination. These findings highlight dopant-distribution engineering as a design principle beyond gap narrowing.

Credits to Mr Ryusei Morimoto for the cover art.

Image reproduced by permission of Ryusei Morimoto from *Phys. Chem. Chem. Phys.*, 2026, **28**, 5111.

As featured in:

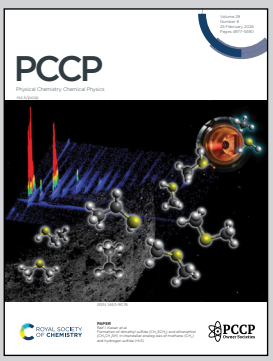

See Hiroki Uratani *et al.*, *Phys. Chem. Chem. Phys.*, 2026, **28**, 5111.

PCCP

PAPER

View Article Online
View Journal | View Issue

Cite this: *Phys. Chem. Chem. Phys.*, 2026, **28**, 5111

Dopant distributions and band-edge positions in Sr-doped $NaTaO_3$: a first-principles study

Ryusei Morimoto, [a] Hiroki Uratani, *[ab] Hiroshi Onishi [cde] and Hirofumi Sato [af]

Received 13th November 2025,
Accepted 18th January 2026

DOI: 10.1039/d5cp04385a

rsc.li/pccp

Sr doping is known to enhance the water-splitting activity of $NaTaO_3$ photocatalysts and is often accompanied by surface segregation of Sr, yet, the electronic-structural origin remains unclear. Here, we employ first-principles calculations with explicit enumeration of all Sr configurations in bulk $NaTaO_3$ (NTO) and TaO_2-terminated (001) surfaces. In the bulk, the enumeration shows that shorter Sr–Sr separations are energetically preferred. At surfaces, Sr segregates and accumulates strongly. Layer-resolved local density of states indicates that in-gap states are confined to the outermost TaO_2 layer, while interior layers retain a near-bulk gap. In Sr-rich surface layers, both band edges shift upward relative to the interior. Population analyses link the valence-band rise to O–O contraction and the conduction-band rise to Ta–Ta elongation. Sr-doping and segregation yields near-surface band bending and a built-in electric field that can promote electron–hole separation and suppress recombination, rationalising the observed activity gains.

Introduction

The breakthrough TiO_2 photoelectrolysis reported by Honda and Fujishima initiated systematic studies of photocatalysis.[1–4] Under above-gap excitation, nonequilibrium electrons and holes are generated, and their behaviour is governed by the electronic structure. In particulate systems, these excited carriers are guided to catalytic sites by several factors such as internal electric fields and diffusion.[5,6] Thus, achieving high efficiency requires an appropriate balance of these mechanisms rather than optical absorption alone.

For overall water splitting, metal-oxide photocatalysts, including $SrTiO_3$,[7,8] $KTaO_3$,[9,10] and $NaTaO_3$,[9,10] are often selected because they satisfy both thermodynamic alignment and chemical stability. In these oxides, aliovalent doping with Sr^{2+},[11,12] La^{3+},[13,14] and Al^{3+} [15,16] has also been employed to further enhance the reaction rate. Although such dopants can modify carrier densities, band-edge positions, and related properties, it is challenging to isolate the dominant mechanism in a given composition because several effects change simultaneously. Moreover, substitutional doping is configurational. Even at fixed compositions, many symmetry-inequivalent dopant arrangements and associated relaxations exist; therefore, assessing dopant effects requires explicit configuration enumeration.[17,18]

In the present study, we focus on the role of dopants in $NaTaO_3$ (NTO), a long-studied ultraviolet (UV)-active perovskite. Among reported dopants for NTO, Sr offers a useful probe of mechanism: substantial rate enhancements have been reported despite only modest shifts in the optical onset without invoking oxygen vacancies.[19,20] Notably, at low Sr concentrations, Sr has been observed to segregate toward the surface and to form Sr-concentration gradients.[21] However, it remains unclear whether the enhanced activity derives primarily from band-edge realignment, mid-gap states, or modified interfacial fields.

Here, we use first-principles calculations on bulk NTO and TaO_2-terminated surfaces to isolate the effects of Sr substitution. Configuration enumeration and energetic screening are performed for all possible Sr configurations in given compositions. Short Sr–Sr separations are energetically favoured, implying a thermodynamic drive toward dopant accumulation. When Sr enriches near the surface or forms Sr-rich layers in the bulk, two coupled responses emerge: (i) acceptor-like in-gap states localised on O atoms adjacent to Sr-perturbed TaO_6 octahedra and (ii) upward shifts of both band edges. The resulting near-surface band bending establishes a built-in electric field that is expected to promote electron–hole separation and suppress

[a] *Department of Molecular Engineering, Graduate School of Engineering, Kyoto University, Nishikyo-ku, Kyoto, 615-8510, Japan. E-mail: uratani@moleng.kyoto-u.ac.jp*
[b] *PRESTO, Japan Science and Technology Agency (JST), Kawaguchi, Saitama, 332-0012, Japan*
[c] *Department of Chemistry, Graduate School of Science, Kobe University, Nada-ku, Kobe, 657-8501, Japan*
[d] *Research Center for Membrane and Film Technology, Kobe University, Nada-ku, Kobe, 657-8501, Japan*
[e] *Division of Advanced Molecular Science, Institute for Molecular Science, Okazaki, 444-8585, Japan*
[f] *Fukui Institute for Fundamental Chemistry, Kyoto University, Sakyo-ku, Kyoto, 606-8103, Japan*

recombination, rationalising activity gains that cannot be explained by band-gap changes alone. These insights suggest a design principle for doped perovskite photocatalysts: controlling dopant distributions and the attendant lattice distortions to engineer band-edge positions and interfacial fields.

Methods

The structural models were constructed as follows. An orthorhombic (*Pnma*) unit cell of NTO was optimised. Based on this cell, we constructed four bulk supercells, 1 × 1 × 3, 1 × 1 × 5, 2 × 2 × 2, and 2 × 2 × 5, as shown in Fig. 1, hereafter denoted as **B1**, **B2**, **B3**, and **B4**, respectively. Sr substitution was introduced using a charge-neutral **3Na1Ta** scheme, in which three Na sites and one Ta site in a given supercell were replaced by Sr, consistent with $NaTaO_3$–$Sr(Sr_{1/3}Ta_{2/3})O_3$ stoichiometry. In each size of supercells except **B4**, all possible Sr (**3Na1Ta**) configurations are considered (details for construction methods are shown in the SI). For **B3**, we also examined four additional patterns: **B3-1Ta** (a Ta site substituted by Sr), **B3-1Na** (a Na site substituted by Sr), **B3-1Ta-c**, and **B3-1Na-c**. In the "**-c**" models, the total number of valence electrons was adjusted to compensate the nominal charge imbalance caused by Sr substitution at only Na or Ta sites. To model the surfaces, we constructed both symmetric and asymmetric slabs. The symmetric slab **S1** consists of a 1 × 1 × 10 supercell with TaO_2-terminated (001) surfaces on both sides and a 15 Å vacuum region. Within this geometry, we considered **S1-2Ta** (two Ta sites substituted by Sr) and **S1-4Na2Ta** (four Na sites and two Ta sites substituted by Sr to maintain charge neutrality). The asymmetric slab **S2** consists of a 1 × 1 × 5 supercell with a TaO_2-terminated surface on one side and a NaO-terminated surface on the other, separated by a 15 Å vacuum layer.

All first-principles calculations used the projector augmented-wave (PAW) method as implemented in the Vienna *ab initio* simulation package.[22] The plane-wave cutoff was set to 400 eV. Unless otherwise noted, exchange–correlation effects were described by Perdew–Burke–Ernzerhof (PBE) generalised-gradient approximation.[23] To assess the impact of nonlocal exchange on the electronic structure, for some cases, we also performed calculations using the hybrid functional HSE06.[24] Spin-polarized calculations were tested but the systems converged to a negligible magnetic moment and showed no meaningful changes in the relevant electronic properties (see Table S1). Therefore, in what follows, the non-spin-polarized calculation results are reported. Brillouin-zone sampling was conducted employing Monkhorst–Pack meshes of 5 × 5 × 2, 3 × 3 × 1, 2 × 2 × 2, and 2 × 2 × 1 for **B1**, **B2**, **B3**, and **B4**, respectively; for slab models, a 3 × 3 × 1 mesh was employed. Dispersion interactions were included for the slab models, using Grimme's D3 correction to PBE (PBE-D3).[25] The convergence criterion for electronic self-consistent field calculations was set to 10^{-7} eV. All structures were relaxed until residual forces were under 0.01 eV $Å^{-1}$, unless otherwise noted. For NTO unit cell and bulk supercell models, no geometric parameters were fixed. For symmetric slabs, the central TaO_2 layer was fixed to emulate a bulk-like interior. For asymmetric slabs, the bottom NaO layer was fixed, and a dipole correction along the surface normal was applied. The projected crystal orbital Hamilton population (pCOHP) was employed as implemented in the LOBSTER package.[26,27] Density of states and band structures were processed with PyProcar.[28] For doped supercells, band structures were analysed using band-structure unfolding to obtain the effective band dispersion in the primitive cell Brillouin zone, following established procedures.[29,30] The unfolding was performed with PyProcar. Crystal structures and charge densities were visualised using VESTA.[31]

Results and discussion

Bulk

To identify low-energy Sr configurations in bulk NTO, we generated all possible Sr configurations and evaluated single-point energies on unrelaxed structures. We considered 110 configurations for **B1-3Na1Ta**, 570 for **B2-3Na1Ta**, and 792 for **B3-3Na1Ta**. Fig. 2 shows the relative energies of unrelaxed **B3-3Na1Ta** configurations as a function of Sr–Sr distances (results for **B1-3Na1Ta** and **B2-3Na1Ta** are shown in Fig. S1 and S2). In **B3-3Na1Ta**, the energy correlates with the Sr–Sr distance, although the shortest separation was not the global minimum and lies 0.3 eV above it; the lowest energy configuration is 2.3 eV below the most separated

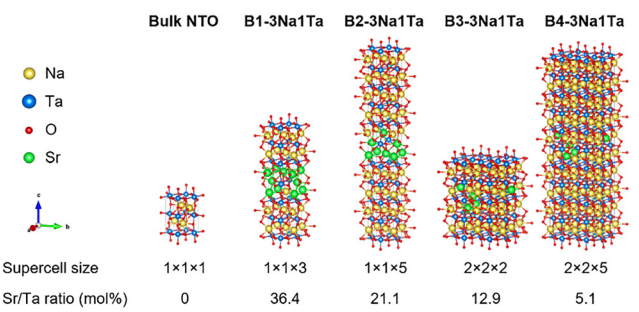

Fig. 1 Representative **3Na1Ta** configurations selected from the enumerated set for Sr-doped $NaTaO_3$ bulk supercells. Sr, green; Na, yellow; Ta, blue; O, red.

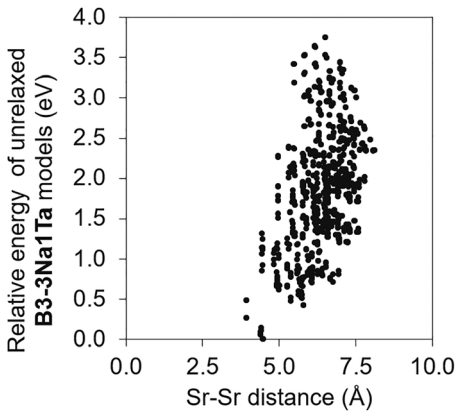

Fig. 2 Sr–Sr distance dependence of relative energy for **B3-3Na1Ta**.

case. For **B1-3Na1Ta** and **B2-3Na1Ta**, the configurations with the shortest Sr–Sr separation are the most stable, lying 3.8 eV and 4.2 eV below the most separated cases, respectively. Overall, shorter Sr–Sr separations are energetically favoured.

From the enumeration, we selected the lowest energy **3Na1Ta** configuration for each supercell. We also built **B4-3Na1Ta** by adopting the minimum-energy arrangement identified in **B3-3Na1Ta**. These structures were then fully relaxed and their atomic coordinates are provided in the SI. Fig. 3 summarises the Sr content and the optimised lattice volume for the **3Na1Ta** models (corresponding lattice parameters are shown in Table S2). All models showed an approximately isotopic expansion with increasing Sr content. For pristine NTO, the calculated lattice volume agrees with experiment within ~0.7%. At 36.4 mol% of Sr (**B1-3Na1Ta**), the cell volume increased by 4.8% relative to pristine NTO.

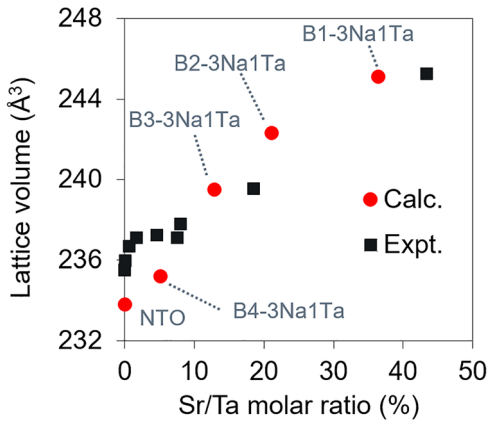

Fig. 3 Lattice volume of Sr-doped $NaTaO_3$ as a function of the nominal Sr/Ta molar ratio. Red circles: DFT-optimised structures (this work). Black squares: experimental values in ref. 20.

Linear dependence between the Sr content and the lattice volume in $NaTaO_3$–$Sr(Sr_{1/3}Ta_{2/3})O_3$ solid solutions has been reported previously.[20] In that work, the lattice volume increased by ~20% from NTO to 200 mol% of Sr. This trend suggests a ~2.0% increase at 21.1 mol% Sr (**B2-3Na1Ta**), which is qualitatively consistent with our computations.

We also examined how the Sr substitution site affects the lattice parameters of **B3-1Ta** and **B3-1Na** (the details are summarised in Table S3). Replacing Ta by Sr expands the lattice more than replacing Na by Sr. Charge compensation had only a minor effect on the lattice parameters (<0.9% in volume).

The lattice expansion may be driven by the difference in ionic radii between the substituting Sr^{2+} and the host cation at the substituted site. Na^+ (~1.39 Å) and Sr^{2+} (~1.44 Å) have similar sizes at the A site, whereas Sr^{2+} (~1.18 Å) is substantially larger than Ta^{5+} (~0.64 Å) at the B site;[32] this mismatch explains stronger expansion for Sr at Ta sites.

The electronic structures of relaxed NTO and Sr-doped NTO were investigated. Fig. 4a shows the total and projected density of states (PDOS) for NTO, **B2-3Na1Ta**, and **B4-3Na1Ta** (other results are provided in Fig. S3a). In all cases, states near the valence-band maximum (VBM) are dominated by O 2p orbitals, while states near the conduction-band minimum (CBM) are dominated by Ta 5d orbitals. Sr-derived states do not appear near the Fermi level even at the highest Sr content; they do not contribute to the band edges.

Fig. 4b shows the band structures of these models (results for other models in Fig. S3b). NTO showed a calculated band gap of 2.80 eV. The lower Sr-content models, **B3-3Na1Ta** and **B4-3Na1Ta**, have slightly smaller gaps of ~2.79 eV and ~2.75 eV,

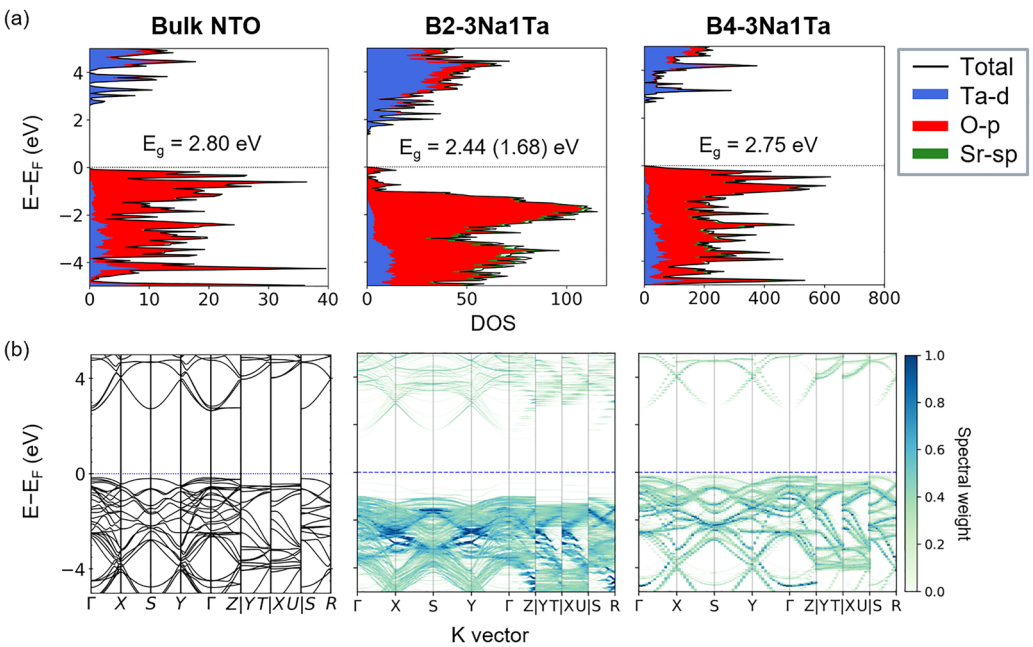

Fig. 4 (a) PDOS for bulk NTO, **B2-3Na1Ta**, and **B4-3Na1Ta**. Total DOS (black line), Ta (blue), O (red), and Sr (green); energies referenced to Fermi energy. (b) Unfolded band structures where the colour indicates the spectral weight.

respectively. These models exhibit no in-gap impurity states. Conversely, the higher Sr-content models, **B1-3Na1Ta** and **B2-3Na1Ta**, exhibit several in-gap impurity states associated with Sr substitution. As indicated by the PDOS in Fig. 4a, acceptor-like levels appear just above the VBM. When in-gap impurity states are ignored, the gaps are 2.74 eV for **B1-3Na1Ta** and 2.44 eV for **B2-3Na1Ta**.

Impurity bands appear owing to Sr accumulation within a TaO_2 layer. In **B1-3Na1Ta** and **B2-3Na1Ta**, an Sr(Ta)O_6 octahedron (Sr at the Ta site, hereafter Sr(Ta)) is fully surrounded by Sr atoms. This locally Sr-rich environment promotes electron localisation and yields in-gap states. The charge distribution for these impurity bands is localised on O atoms adjacent to the Sr(Ta)O_6 octahedra (see Fig. S4 and S5). Although Sr tends to accumulate also in **B3-3Na1Ta**, this cell does not contain the Sr(Ta)O_6 octahedron fully surrounded by Sr at neighbouring A sites. Accordingly, charge localisation is weaker in **B3-3Na1Ta** than in **B1-3Na1Ta** and **B2-3Na1Ta**.

The DOS of NTO, **B1-3Na1Ta**, **B2-3Na1Ta**, and **B3-3Na1Ta** were also computed using HSE06 (Fig. S6). The resulting gap of NTO was about 4.35 eV, which is in better agreement with the experimental value (4.0 eV) than the PBE result.[9,33] A similar change in the band gap was observed for **B1-3Na1Ta**, **B2-3Na1Ta**, and **B3-3Na1Ta**. The overall DOS features, including the in-gap states, remained qualitatively unchanged compared with PBE. These results suggest that while the use of hybrid functionals improves the quantitative band-gap value, the key electronic-structure trends discussed here are robust with respect to the choice of the functional.

Experimentally, An *et al.* reported that in $NaTaO_3$–Sr($Sr_{1/3}Ta_{2/3}$)O_3 solid solutions the optical band gap increases with Sr content (UV-vis).[20] By contrast, our supercell calculations predict a decreasing gap at higher Sr contents and, when Sr accumulates, the in-gap states emerge. This discrepancy likely reflects the limitations of finite periodic supercells. As indicated by Caldes *et al.*,[34] Sr atoms and Ta atoms are mixed in Sr($Sr_{1/3}Ta_{2/3}$)O_3 (200 mol% Sr *vs.* Ta). Random solid solutions require configurational averaging over fractional compositions, which small periodic supercells cannot represent adequately. Consequently, artificial Sr ordering/clustered environments, the absence of configurational averaging, and finite-size effects in small supercells likely bias the computed gap relative to the experiment.

Surface

We also examined the Sr configurations in surface slab models. As reported by Zhao and Selloni,[35] various surface termination exist. Here, we focus on bare (clean) surfaces without H_2O or H adsorption. We used TaO_2 terminated symmetric slabs, reported to be the most stable termination without steps and H_2O.[35] First, to probe favourable Sr sites, we performed single-point calculations for **S1-2Ta**. We compared five configurations (**a-e**, Fig. 5a) that systematically vary the Sr depth from the surface top. As shown in Fig. 5b, the total energy decreases as Sr approaches the surface, by up to 5.8 eV relative to the deepest configuration.

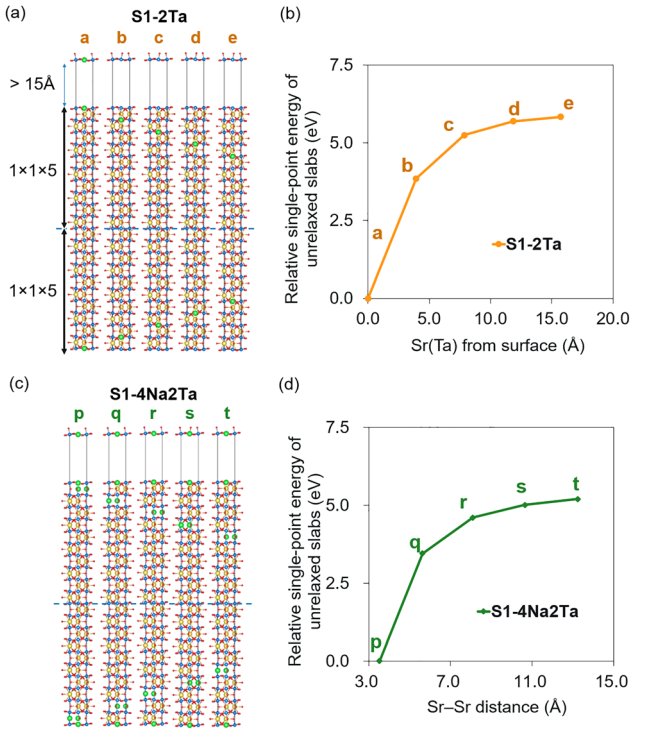

Fig. 5 (a) Symmetric 1 × 1 × 10 TaO_2-terminated slabs with two Sr substitutions at Ta sites (**S1-2Ta**). (b) Relative unrelaxed single-point energies of **S1-2Ta** with respect to the Sr distance from the top surface. (c) Symmetric 1 × 1 × 10 TaO_2-terminated slabs with six Sr substitutions at four Na sites and two 2Ta sites (**S1-4Na2Ta**). (d) Relative unrelaxed single-point energies of **S1-4Na2Ta** configurations with respect to the Sr–Sr distance.

Starting from the most stable **S1-2Ta** configuration (**a**), we constructed **S1-4Na2Ta** slabs by additionally replacing four Na sites with Sr (**p-t**, Fig. 5c), and varied the Sr(Na) depth across five configurations. The **S1-2Ta** slabs have excess electrons due to the termination and substitution, but the **S1-4Na2Ta** slabs do not. As in the bulk, shorter Sr–Sr separations stabilise the surface: across the five **S1-4Na2Ta** configurations, and the most concentrated arrangement is lower by 5.2 eV than the most dispersed one (Fig. 5d). This result indicates a tendency for Sr to segregate on the surface, being consistent with earlier EDX mapping reports of Sr surface segregation.[21]

To exclude artefacts arising from the slab construction, including spurious Sr–Sr interactions between periodically repeated slabs in **S1-2Ta** and **S1-4Na2Ta**, we performed two checks. First, the vacuum thickness was increased from 15 Å to 31 Å; the relative energies remained essentially unchanged over this range (Fig. S7). Second, we computed asymmetric, stoichiometric slabs constructed from a 1 × 1 × 5 unit cell with NaO- and TaO_2-terminated surfaces separated by a vacuum layer (**S2-1Ta** and **S2-3Na1Ta**). Consistent with the symmetric slabs, the energy increases as Sr is placed deeper toward the slab interior (see Fig. S8 for details). Thus, the preference for Sr at the surface (and the corresponding destabilisation when Sr is buried) does not originate from stoichiometry or charge-compensation effects; it persists in asymmetric, stoichiometric slabs as implied in previous study.[33]

Table 1 Bader charges for unrelaxed slabs

Structure	Distance between Sr(Ta) and Sr(Na) layers (Å)	Bader charges			
		O near Sr(Ta)	O near Na)	Sr(Ta)	Sr(Na)
NTO slab		−1.29	−1.29		
S1-4Na2Ta (p)	1.94	−1.22	−1.28	+1.52	+1.53
S1-4Na2Ta (t)	17.48	−1.03	−1.35	+1.59	+1.53

Table 1 shows Bader charges for the **NTO slab** and **S1-4Na2Ta** variants **p** and **t** (Fig. 5b). Relative to the undoped slab, O atoms adjacent to Sr(Ta) are less negative, whereas O atoms adjacent to Sr(Na) are more negative. The magnitude of both shifts is larger in **t** than in **p**. This trend reflects local charge compensation upon the Sr substitution. Sr has two valence electrons, whereas Ta and Na have five and one, respectively. When a Ta site is substituted by Sr (Sr(Ta)), the local region contains fewer electrons than in pristine NTO; when a Na site is substituted by Sr (Sr(Na)), the local region contains more electrons. Consistent with this simple electron-counting picture, O atoms adjacent to Sr(Ta) show less negative Bader charges, and O atoms adjacent to Sr(Na) show more negative Bader charges. When Sr(Ta) and Sr(Na) are close (**p**), the local electron deficit and excess can partially compensate, whereas at longer separation (**t**) this compensation is weaker. This local charge compensation accounts for the greater stability of **p** relative to **t**. A similar trend in Bader charges is observed for the bulk (Table S4). The correlation between the mean Sr(Na)–Sr(Ta) separation and the single-point energy is stronger than that for Sr(Na)–Sr(Na) or any Sr–Sr separations (Fig. S9–S11), supporting the stabilisation mechanism of **p** relative to **t**.

In subsequent analyses, we focused on the minimum-energy **S1-2Ta** and **S1-4Na2Ta** configurations (**a** and **p**, respectively); we optimised ionic positions with the central unit cell constrained to maintain the symmetric slab geometry. Electronic DOS for **NTO slab**, **S1-2Ta**, and **S1-4Na2Ta** are shown in Fig. 6a, and the corresponding band structures are presented in Fig. S12. As in the bulk, states near the VBM are dominated by O 2p orbitals, and those near the CBM by Ta 5d orbitals. No Sr derived states are observed near the Fermi energy. For the **NTO slab** and **S1-2Ta**, shallow in-gap states appear within ∼+0.6 eV above the VBM. In contrast, the stoichiometric **S1-4Na2Ta** exhibits deeper impurity states at ∼+2.0 eV above the VBM, localised on O atoms neighbouring Sr(Ta) (see Fig. S13). If we set aside these strongly localised defect states, which are unlikely to contribute to carrier transport, and estimate the underlying band edges from the PDOS, the apparent gaps are 2.70 eV for NTO (within ∼0.1 eV of the bulk), 2.69 eV for **S1-2Ta**, and ∼2.76 eV for **S1-4Na2Ta**. Similar results were obtained for **S1-4Na2Ta** using HSE06 (Fig. S14).

We further analysed the local density of states (LDOS) layer-by-layer for the TaO_2 planes parallel to (001). Fig. 6b shows the TaO_2 layer-resolved LDOS for the **NTO**, **S1-2Ta**, and **S1-4Na2Ta** slabs. For all models, L2 to L11 show nearly identical gaps

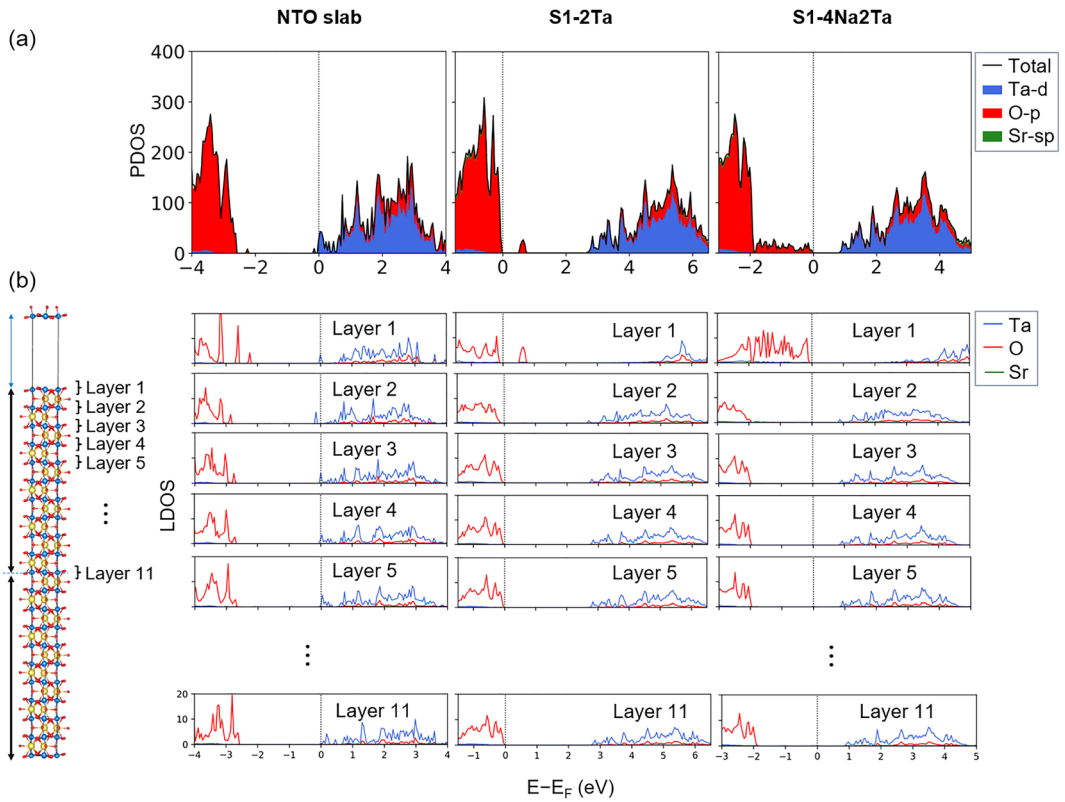

Fig. 6 (a) Total DOS and PDOS for the relaxed **NTO slab**, **S1-2Ta**, and **S1-4Na2Ta**; energies referenced to Fermi energy. (b) Layer-resolved LDOS for slabs.

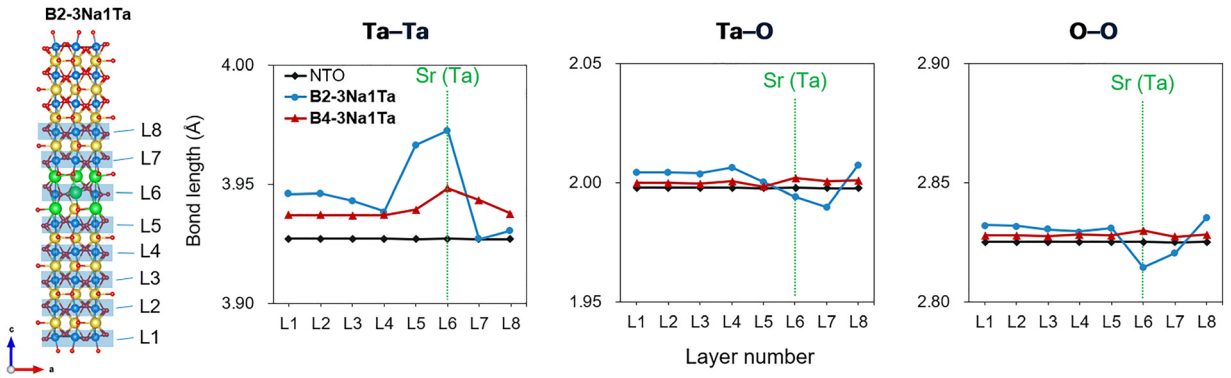

Fig. 7 Layer-resolved bond length for bulk models.

without any in-gap states. In the surface layer (L1), however, the behaviour changes. For the VBM, NTO and **S1-2Ta** showed shallow in-gap states within ~0.6 eV above the VBM. These shallow in-gap states are consistent with the non-stoichiometric termination. By contrast, **S1-4Na2Ta** showed deeper in-gap states (~2.0 eV above the VBM) despite its stoichiometric composition. For the CBM, the NTO surface layer closely matches the interior. However, in **S1-2Ta** and **S1-4Na2Ta**, the conduction band edges are shifted upward by approximately 2.5 eV relative to interior layers. Therefore, Sr substitution at Ta sites raises the surface CBM, and that additional Sr substitution at Na sites (Sr segregation) elevates both the VBM and the CBM relative to interior layers.

Similar upward shifts of the VBM and CBM are observed in bulk supercells with Sr accumulation around Sr(Ta) in **B1-3Na1Ta** and **B2-3Na1Ta** (see Fig. S15–S17). In **B1-3Na1Ta** and **B2-3Na1Ta**, the Sr-rich layer showed upward shifting of the VBM and CBM. **B3-3Na1Ta** and **B4-3Na1Ta** also showed upward shifts, with reduced contribution from the O 2p near VBM and Ta 5d near the CBM, although the magnitude is smaller than the other models.

To probe the origin of the upward VBM/CBM shifts, we analysed bond lengths in each TaO_2 layers and computed pCOHP. In **B2-3Na1Ta**, Fig. 7 indicates that Ta–Ta bond lengths are elongated near the Sr accumulated layer, whereas the O–O and Ta–O distances are shortened. By contrast, **B4-3Na1Ta** showed smaller layer-to-layer variations. In **S1-4Na2Ta** as well, Ta–Ta lengths are elongated and O–O and Ta–O lengths are shortened at the surface (Fig. S18).

Fig. 8 shows pCOHP for the NTO surface, **B2-3Na1Ta**, and **S1-4Na2Ta**. All models show similar features; O–O antibonding contributions appear near the VBM, while Ta–O antibonding and Ta–Ta bonding contributions appear near the CBM. The in-gap states in the **S1-4Na2Ta** model are contributed from O–O antibonding and Ta–O antibonding characters.

Fig. 9 schematically illustrates a possible mechanism of the band-edge shifts. Shortening of O–O distances enhances O–O antibonding interactions near the VBM, shifting the VBM upward. Elongation of Ta–Ta distances weakens Ta–Ta bonding interactions and, shortening Ta–O length increases Ta–O antibonding interactions, effectively shifting the CBM upward. Sr accumulation at the surface also reduces Ta–Ta overlap, particularly near the conduction-band edge. Consequently, both the VBM and the CBM shift upward toward the surface owing to these local structural changes.

Layer-localised band-edge shifts correspond to band bending near the surface, as suggested previously. Previous studies assumed that only the CBM shifts upward toward the surface,

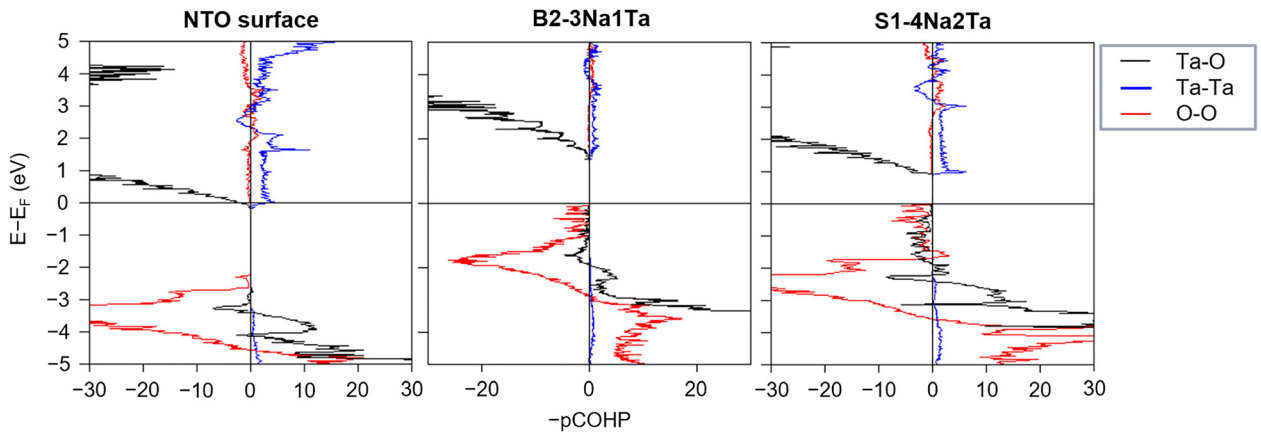

Fig. 8 pCOHP for the NTO surface, **B2-3Na1Ta**, and **S1-4Na2Ta**.

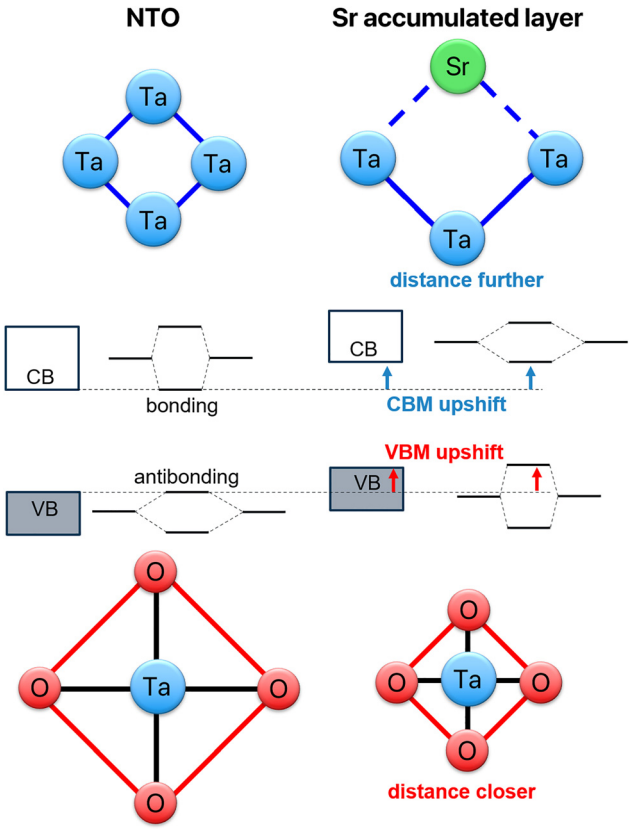

Fig. 9 Schematic of the band-bending mechanism at Sr-rich layers.

producing internal band bending that suppresses electron–hole recombination.[19,21] In our calculations, the CBM shifts upward as the TaO_2 layer approaches the surface from the interior. In addition, we found that the VBM shifts upward as well in the Sr segregated model. The concurrent upward shifts of the CBM and VBM establish a built-in electric field across the near-surface region. This field drives electron–hole separation and suppresses recombination. As a result, carrier lifetimes increase, enhancing the availability of electrons and holes for interfacial redox reactions with water.

Conclusions

Using first-principles calculations, we systematically examined Sr substitution in the bulk and TaO_2-terminated surfaces of $NaTaO_3$ (NTO). Enumeration and screening of configurations showed that shorter Sr–Sr separations are energetically favoured, and the lattice volume increases monotonically with Sr content. Substitution at Ta (B) sites expands the lattice more than that at Na (A) sites, consistent with ionic radii. At lower Sr contents, the gap is comparable to that of pristine NTO (2.80 eV), whereas Sr accumulation (*e.g.*, $1 \times 1 \times 3$ and $1 \times 1 \times 5$; $Sr(Ta)O_6$ surrounded by Sr at A sites) produces in-gap acceptor-like states near the VBM and reduces the host gap.

At the surface, Sr segregates strongly and tends to accumulate, which is a trend that is robust to slab stoichiometry and charge compensation. Layer-resolved LDOS shows that in-gap states are confined to the outermost TaO_2 layer, while interior layers retain a nearly constant gap. In both **S1-2Ta** and **S1-4Na2Ta** slabs, the VBM and CBM shift upward in the surface layer relative to the interior; similar band-edge upshifts appear in Sr-rich layers of bulk supercells. Analysis of bond metrics and pCOHP links these shifts to O–O contraction (enhanced O–O antibonding raising the VBM) and Ta–Ta elongation together with Ta–O antibonding (raising the CBM).

These results establish a near-surface band bending driven by local Sr-induced structural distortions, creating a built-in electric field that promotes electron–hole separation and suppresses recombination, thereby enhancing photo-driven water splitting on Sr-modified NTO.

Conflicts of interest

There are no conflicts to declare.

Data availability

The data supporting the findings of this study are presented in the main text and supplementary information (SI). Supplementary information: supporting figures and tables (PDF), and atomic coordinates used for the calculations (VASP POSCAR format). See DOI: https://doi.org/10.1039/d5cp04385a.

Acknowledgements

This study was financially supported by the JSPS-KAKENHI (Grant No. 23H03976 and 25H00902), JST-PRESTO (Grant No. JPMJPR23Q2), Toyota Physical and Chemical Research Institute, Japan, and Institute for Quantum Chemical Exploration, Japan. Theoretical computations were partly performed in Research Center for Computational Science, Okazaki, Japan (25-IMS-C019) and Research Institute for Information Technology, Kyushu University, Japan (p240303346).

References

1 A. Fujishima and K. Honda, Electrochemical Photolysis of Water at a Semiconductor Electrode, *Nature*, 1972, **238**, 37–38.
2 Z. Zhang and J. T. Yates, Band Bending in Semiconductors: Chemical and Physical Consequences at Surfaces and Interfaces, *Chem. Rev.*, 2012, **112**, 5520–5551.
3 A. Kudo and Y. Miseki, Heterogeneous photocatalyst materials for water splitting, *Chem. Soc. Rev.*, 2008, **38**, 253–278.
4 K. Maeda and K. Domen, Photocatalytic Water Splitting: Recent Progress and Future Challenges, *J. Phys. Chem. Lett.*, 2010, **1**, 2655–2661.
5 T. Hisatomi, J. Kubota and K. Domen, Recent advances in semiconductors for photocatalytic and photoelectrochemical water splitting, *Chem. Soc. Rev.*, 2014, **43**, 7520–7535.

6 S. Zhu and D. Wang, Photocatalysis: Basic Principles, Diverse Forms of Implementations and Emerging Scientific Opportunities, *Adv. Energy Mater.*, 2017, **7**, 1700841.
7 A. Kudo, A. Tanaka, K. Domen and T. Onishi, The effects of the calcination temperature of $SrTiO_3$ powder on photocatalytic activities, *J. Catal.*, 1988, **111**, 296–301.
8 K. Domen, S. Naito, M. Soma, T. Onishi and K. Tamaru, Photocatalytic decomposition of water vapour on an NiO–$SrTiO_3$ catalyst, *J. Chem. Soc., Chem. Commun.*, 1980, 543–544.
9 H. Kato and A. Kudo, Water Splitting into H_2 and O_2 on Alkali Tantalate Photocatalysts $ATaO_3$ (A = Li, Na, and K), *J. Phys. Chem. B*, 2001, **105**, 4285–4292.
10 H. Kato and A. Kudo, New tantalate photocatalysts for water decomposition into H_2 and O_2, *Chem. Phys. Lett.*, 1998, **295**, 487–492.
11 A. Iwase, H. Kato, H. Okutomi and A. Kudo, Formation of Surface Nano-step Structures and Improvement of Photocatalytic Activities of $NaTaO_3$ by Doping of Alkaline Earth Metal Ions, *Chem. Lett.*, 2004, **33**, 1260–1261.
12 H. Kadowaki, N. Saito, H. Nishiyama and Y. Inoue, RuO_2-loaded Sr^{2+}-doped CeO_2 with d^0 Electronic Configuration as a New Photocatalyst for Overall Water Splitting, *Chem. Lett.*, 2007, **36**, 440–441.
13 A. Kudo and H. Kato, Effect of lanthanide-doping into $NaTaO_3$ photocatalysts for efficient water splitting, *Chem. Phys. Lett.*, 2000, **331**, 373–377.
14 H. Kato, K. Asakura and A. Kudo, Highly Efficient Water Splitting into H_2 and O_2 over Lanthanum-Doped $NaTaO_3$ Photocatalysts with High Crystallinity and Surface Nanostructure, *J. Am. Chem. Soc.*, 2003, **125**, 3082–3089.
15 Y. Goto, *et al.*, A Particulate Photocatalyst Water-Splitting Panel for Large-Scale Solar Hydrogen Generation, *Joule*, 2018, **2**, 509–520.
16 T. H. Chiang, *et al.*, Efficient Photocatalytic Water Splitting Using Al-Doped $SrTiO_3$ Coloaded with Molybdenum Oxide and Rhodium–Chromium Oxide, *ACS Catal.*, 2018, **8**, 2782–2788.
17 S. Kasamatsu, O. Sugino, T. Ogawa and A. Kuwabara, Dopant arrangements in Y-doped $BaZrO_3$ under processing conditions and their impact on proton conduction: a large-scale first-principles thermodynamics study, *J. Mater. Chem. A*, 2020, **8**, 12674–12686.
18 F. Tian, A Review of Solid-Solution Models of High-Entropy Alloys Based on Ab Initio Calculations, *Front. Mater.*, 2017, **4**, 36.
19 H. Onishi, Sodium Tantalate Photocatalysts Doped with Metal Cations: Why Are They Active for Water Splitting?, *ChemSusChem*, 2019, **12**, 1825–1834.
20 L. An and H. Onishi, Electron–Hole Recombination Controlled by Metal Doping Sites in $NaTaO_3$ Photocatalysts, *ACS Catal.*, 2015, **5**, 3196–3206.
21 L. An, *et al.*, Photoexcited Electrons Driven by Doping Concentration Gradient: Flux-Prepared $NaTaO_3$ Photocatalysts Doped with Strontium Cations, *ACS Catal.*, 2018, **8**, 9334–9341.
22 G. Kresse and J. Furthmüller, Efficiency of ab-initio total energy calculations for metals and semiconductors using a plane-wave basis set, *Comput. Mater. Sci.*, 1996, **6**, 15–50.
23 J. P. Perdew, K. Burke and M. Ernzerhof, Generalized Gradient Approximation Made Simple, *Phys. Rev. Lett.*, 1996, **77**, 3865–3868.
24 J. Heyd, G. E. Scuseria and M. Ernzerhof, Erratum: ''Hybrid functionals based on a screened Coulomb potential'' [*J. Chem. Phys.* **118**, 8207 (2003)], *J. Chem. Phys.*, 2006, **124**, 219906.
25 S. Grimme, S. Ehrlich and L. Goerigk, Effect of the damping function in dispersion corrected density functional theory, *J. Comput. Chem.*, 2011, **32**, 1456–1465.
26 V. L. Deringer, A. L. Tchougréeff and R. Dronskowski, Crystal Orbital Hamilton Population (COHP) Analysis As Projected from Plane-Wave Basis Sets, *J. Phys. Chem. A*, 2011, **115**, 5461–5466.
27 S. Maintz, V. L. Deringer, A. L. Tchougréeff and R. Dronskowski, LOBSTER: A tool to extract chemical bonding from plane-wave based DFT, *J. Comput. Chem.*, 2016, **37**, 1030–1035.
28 U. Herath, *et al.*, PyProcar: A Python library for electronic structure pre/post-processing, *Comput. Phys. Commun.*, 2020, **251**, 107080.
29 Z. Wang, J. Zhang and H. Du, Achieving the Sensing Property of Hg^0 Molecules on Black Phosphorene Nanosheets Using Anisotropy as a Response Signal, *ACS Appl. Nano Mater.*, 2025, **8**, 8417–8423.
30 V. Popescu and A. Zunger, Extracting *E versus* $\vec{P}$ effective band structure from supercell calculations on alloys and impurities, *Phys. Rev. B: Condens. Matter Mater. Phys.*, 2012, **85**, 085201.
31 K. Momma and F. Izumi, VESTA 3 for three-dimensional visualization of crystal, volumetric and morphology data, *J. Appl. Crystallogr.*, 2011, **44**, 1272–1276.
32 R. D. Shannon, Revised effective ionic radii and systematic studies of interatomic distances in halides and chalcogenides, *Acta Crystallogr., Sect. A*, 1976, **32**, 751–767.
33 Z.-K. Tang, C. Di Valentin, X. Zhao, L.-M. Liu and A. Selloni, Understanding the Influence of Cation Doping on the Surface Chemistry of $NaTaO_3$ from First Principles, *ACS Catal.*, 2019, **9**, 10528–10535.
34 M. T. Caldes, *et al.*, Solving modulated structures by X-ray and electron crystallography, *Micron*, 2001, **32**, 497–507.
35 X. Zhao and A. Selloni, Structure and stability of $NaTaO_3$(001) and $KTaO_3$(001) surfaces, *Phys. Rev. Mater.*, 2019, **3**, 015801.

